Applied Catalysis B: Environmental 190 (2016) 1–11

Contents lists available at ScienceDirect

Applied Catalysis B: Environmental

journal homepage: www.elsevier.com/locate/apcatb

Multifunctional photocatalytic performances of recyclable Pd-$NiFe_2O_4$/reduced graphene oxide nanocomposites via different co-catalyst strategy

Yinle Li, Zhuqing Zhang, Liyuan Pei, Xiaoguang Li, Tao Fan, Jin Ji, Jianfeng Shen*, Mingxin Ye*

Institute of Special Materials and Technology, Fudan University, Shanghai 200433, China

ARTICLE INFO

Article history:
Received 9 January 2016
Received in revised form 22 February 2016
Accepted 24 February 2016
Available online 27 February 2016

Keywords:
Graphene
Pd
$NiFe_2O_4$
Dyes degradation
Photocatalytic Suzuki–Miyaura reaction

ABSTRACT

In this report, magnetically recyclable, multifunctional Pd-$NiFe_2O_4$/reduced graphene oxide (Pd-$NiFe_2O_4$/rGO) photocatalysts have been successfully prepared by a one-step green hydrothermal method. The integration of $NiFe_2O_4$ with Pd nanoparticles supported on rGO enables efficient harvesting visible light for different catalytic reactions on the heterojunction structures. The Pd-$NiFe_2O_4$/rGO nanocomposites present significantly enhanced photocatalytic activity toward dyes degradation compared to the blank-$NiFe_2O_4$ and the optimum binary $NiFe_2O_4$/rGO, which is ascribed to the added Pd nanoparticles, acting as the mediator on the interfacial layer between $NiFe_2O_4$ and rGO, and transferring the charge carrier across the heterojunction interface. Another important role of Pd nanoparticles is as the electron reservoir, which can directly trap photogenerated electrons. It is interesting that the photogenerated electrons, which transfer to Pd nanoparticles, can increase the electron density of Pd. The energetic Pd nanoparticles thus raise their intrinsic catalytic activity, which can promote the Suzuki coupling under visible light irradiation. A possible catalytic mechanism for the multifunctional efficient photocatalytic performances is proposed.

1. Introduction

Until now, solar energy is considered as the key to solve environment problems and energy demand [1]. To efficiently harvest solar energy, various kinds of photocatalysts have been invented. Metal oxides or sulfides, such as titanium oxide (TiO_2) [2], zinc oxide (ZnO) [3], tungstic oxide (WO_3) [4], ceria (CeO_2) [5], cadmium sulfide (CdS) [6], stannic oxide (SnO_2) [7] and copper sulfide (CuS) [8], were still considered to be the most efficient and environmentally friendly photocatalysts, by reason of their particular optical, electric and catalytic properties. However, pure metal oxides or sulfides photocatalysts have fatal shortcomings since their relatively narrow band gap (TiO_2, 3.20 eV; ZnO, 3.37 eV; WO_3, 2.8 eV; CeO_2, 2.76 eV; CdS, 2.42 eV) [9], low quantum yield, and the restricted photo-responding range, which indexes that they are not induced to the visible region [10]. Moreover, photocatalytic processes were usually implemented in heterogeneous systems. Recovery and reutilization of photocatalysts are of great importance for green sustainable application. The introduction of magnetic materials in solid matrices allows the integration of well-known procedures for photocatalytic with magnetic separation [11]. In this regard, it is significant to develop magnetic photocatalysts due to their ease recovery by magnetic separation to prevent the loss of catalyst and increase recyclability.

Recently, ferrimagnetism spinel ferrites (MFe_2O_4, M = Ni, Zn, Mn, Cu, Co) show a promising photocatalytic performance and were widely studied, since their narrow band gaps near 2 eV, magnetic separability, and chemically stabilities [12]. However, MFe_2O_4, similar to the metal oxides or sulfides, show a poor photocatalytic activity alone. The main problem is the fast recombination of photogenerated electron-hole pairs. As we all known, graphene (GR) is an ideal platform to accept and transport photogenerated electrons from photocatalyst under the light irradiation, resulting in improving the transfer efficiency and lifetime of photogenerated electrons of photocatalyst [13–15]. Vast GR-based photocatalysts have been well reported, which demonstrated the close interfacial contact between graphene and the photocatalyst, is a key factor in adequately utilizing the electron conductivity of GR to enhance the photocatalytic activity [16–18]. The nanocomposites constituted by MFe_2O_4 and GR, such as $NiFe_2O_4$-GR [19], $ZnFe_2O_4$-GR

* Corresponding authors.
E-mail addresses: jfshen@fudan.edu.cn (J. Shen), mxye@fudan.edu.cn (M. Ye).

http://dx.doi.org/10.1016/j.apcatb.2016.02.054
0926-3373/

[20], $MnFe_2O_4$-GR [21], $CuFe_2O_4$-GR [22], $CoFe_2O_4$-GR [23], have been broadly designed for the fabrication of magnetically separable GR-based photocatalysts. Our team also successfully synthesized rGO-$NiFe_2O_4$ nanocomposites via one-pot polyelectrolyte assisted hydrothermal method to improve the electrochemical and photocatalytic properties [24].

In addition to reinforcing the interfacial contact between GR and photocatalyst, some researchers also highlighted that the optimization of transfer pathway of photogenerated electrons across the interface of graphene-based composites, is an efficient method to boost the photocatalytic performance [25,26]. This can be readily accomplished by importing a small amount of noble metals (such as Au [27], Ag [28], Pd [29], and so on), which act as the intermediators or electron-transfer system on the interfacial matrix between GR and photocatalysts. Additionally, noble metals are also broadly used as electron reservoir to delay the recombination of photogenerated electron-hole pairs of photocatalysts [30]. Moreover, such a sample "electron reservoir" strategy is able to enhance the electron density of noble metals nanoparticles, resulting in raising the intrinsic catalytic activity of noble metals, which can drive the chemical reactions under visible light irradiation [31].

In this report, the ternary Pd-$NiFe_2O_4$/rGO nanocomposites have been prepared by a one-step facile, green hydrothermal method. In the meantime, Zhao and Liu [32] successfully prepared the $NiFe_2O_4$@rGO-Pd nanocomposite by a two-step synthetic method for thermocatalytic Suzuki–Miyaura coupling reactions. However, both the photocatalytic performance of $NiFe_2O_4$ and the special electron transfer and reservoir capabilities of Pd nanoparticles were shielded. In this work, we not only demonstrate that the ternary Pd-$NiFe_2O_4$/rGO nanocomposites show significantly enhanced photocatalytic dyes degradation activity as compared to both blank-$NiFe_2O_4$ and the optimum binary $NiFe_2O_4$/rGO nanocomposites, but also reveal the state-of-the-art photocatalytic capabilities of noble metal Pd nanoparticles, which have formed the very recent fast expansion of basis field of green photocatalysis for organic chemical transformations [33,34]. Thus, this work provides a simple, convenient method for designing multifunctional efficient photocatalysts, which are composed of the photocatalyst and the catalytically active noble metal for various wastewater treatment and organic transformations driven by visible light irradiation.

2. Experimental

2.1. Material synthesis

GO was synthesized according to the Hummers method [24]. The $NiFe_2O_4$/rGO nanocomposites were prepared by a facile hydrothermal method with different amounts of GO (ranges from 0.01 to 0.05 g, with 0.01 g as a step size). In brief, $NiCl_2·6H_2O$ (237.7 mg, 1 mmol) and $FeCl_3$ (324.4 mg, 2 mmol) were dissolved in 20 mL deionized water, and the mixture was stirred for 0.5 h. 10 mg GO was dispersed in 80 mL ethanol under ultrasonic for 0.5 h. After that, it was added to the former solution and continued stirring for 30 min. Then, 6 M NaOH solutions were added until the pH value of the solution reached 10. Then the solution transfer into a 150 mL stainless-steel autoclave and maintained at 180 °C for 20 h. The catalyst was separated from the solution with a magnet and rinsed with water and ethanol twice, and dried in vacuum at 40 °C for 24 h. The product was described as $NiFe_2O_4$/RGO-1. $NiFe_2O_4$/RGO-2, $NiFe_2O_4$/RGO-3, $NiFe_2O_4$/RGO-4 and $NiFe_2O_4$/RGO-5 were obtained with 20, 30, 40 and 50 mg GO. For comparison, $NiFe_2O_4$ was prepared using the same preparation method of $NiFe_2O_4$/RGO without the addition of GO.

The Pd-$NiFe_2O_4$/rGO nanocomposites were prepared with the same method to the $NiFe_2O_4$/rGO with different amounts of GO (ranges from 0.04 to 0.08 g, with 0.01 g as a step size) and K_2PdCl_4 (9.8 mg 0.03 mmol). The whole preparation process is outlined in Scheme 1. The product with 40 mg GO was described as Pd-$NiFe_2O_4$/RGO-1. Pd-$NiFe_2O_4$/RGO-2, Pd-$NiFe_2O_4$/RGO-3, Pd-$NiFe_2O_4$/RGO-4 and Pd-$NiFe_2O_4$/RGO-5 were obtained with 50, 60, 70 and 80 mg GO. For comparison, Pd-$NiFe_2O_4$ was prepared using the same preparation method of Pd-$NiFe_2O_4$/RGO without the addition of GO. Pd/rGO was prepared using the same preparation method of Pd-$NiFe_2O_4$/RGO-4 without the addition of $NiCl_2·6H_2O$ and $FeCl_3$. The Pd-$NiFe_2O_4$/RGO-4 catalyst was decomposed in aqua region for the analysis of ICP-AES to determine the content of Pd (0.85 wt%).

2.2. Photocatalytic degradation measurement

The photocatalytic degradation experiment under visible light irradiation was conducted with a 300 W Xe l

amp. An optical filter (λ > 400 nm) was used to block the UV irradiation. The Photo-Fenton degradation progress was conducted in a 200 mL beaker with the environment temperature of 25 ± 2 °C. 50 mL RhB solution (20 mg/L), 50 mg Pd-$NiFe_2O_4$/rGO were added gradually, and the distance between the UV lamp and test solution was approximately 25 cm. Before visible light illumination, the above suspension was stirred under dark for 1 h to make sure the adsorption-desorption equilibrium between the catalyst and reactant. The UV–vis absorbance of RhB was investigated at regular intervals with a UV–vis spectroscopy (Shimadzu UV-3600).

2.3. Photocatalytic Suzuki reaction

In a typical reaction, 1 mL of water, 9 mL of ethanol, 1 mmol of aryl halide, 1.2 mmol of aryl boronic acid, 2.5 mmol of K_2CO_3 and Pd-$NiFe_2O_4$/RGO (0.5 mmol% Pd) were mixed in a 25 mL round bottom flask. The photocatalytic experiment under visible light irradiation was conducted with a 300 W Xe lamp in N_2 atmosphere. An optical filter (λ > 400 nm) was used to block the UV irradiation. The distance between the lamp and flask were 25 cm. The temperature of the reaction solution was maintained at 25 °C using a water bath during the reaction. The products were extracted with ethyl acetate twice. After purification on a microcolumn filled with silica gel, the products were analyzed by GC–MS (Agilent 5975). Yields were determined by GC, m-xylene was used as the internal standard.

2.4. Thermocatalytic Suzuki reactions

The catalysts with Pd content (0.5 mmol% Pd), K_2CO_3 (2.5 mmol), aryl halide (1.0 mmol) and arylboronic acid (1.2 mmol) were added to a Schlenk tube containing a magnetic stir bar. 5.0 mL of solvent (EtOH/H_2O = 9:1) was added. The mixture was stirred at 80 °C in N_2 atmosphere. We monitored the reaction process by GC at a fixed time interval. After completion of the reaction, the catalyst was separated from the mixture with a magnet, washed several times with water and ethanol, and then dried in vacuum at 60 °C overnight. The resulting solution was extracted by EtOAc three times for GC–MS analysis. Yields were determined by GC, m-xylene was used as the internal standard.

3. Results and discussion

3.1. Formation of Pd-$NiFe_2O_4$/rGO nanocomposites

As described in Scheme 1, the Pd-$NiFe_2O_4$/rGO nanocomposites were synthesized with Fe^{3+} ion source existed in $FeCl_3$, Ni^{2+} in $NiCl_2·6H_2O$ and Pd^{2+} in K_2PdCl_4 in the presence of GO solution.

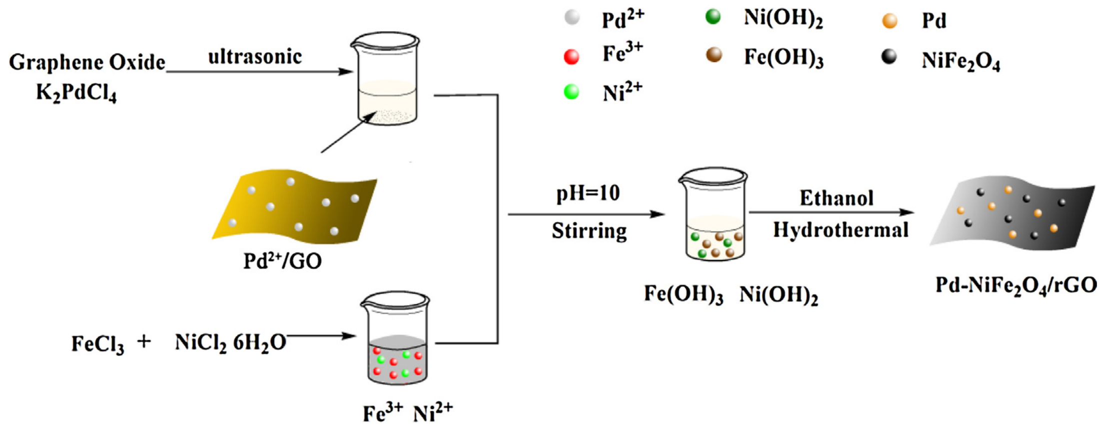

Scheme 1. The preparation route of the Pd-$NiFe_2O_4$/rGO nanocomposites.

Ethanol acts as a reducing agent for the generation of Pd nanoparticles and the reduction of GO under the hydrothermal condition [19]. Both Pd and $NiFe_2O_4$ nanoparticles can be loaded onto the surface of rGO through a green self-assembly way to form Pd-$NiFe_2O_4$/rGO nanocomposites without adding detrimental reductant, surfactant, or stabilizer. The formation of $NiFe_2O_4$ nanoparticles can be represented as followed [35]:

$$Fe^{3+} + 3OH^- \rightarrow Fe(OH)_3$$

$$Fe(OH)_3 \rightarrow \beta\text{-FeOOH}$$

$$Ni^{2+} + 2OH^- \rightarrow Ni(OH)_2$$

$$Ni(OH)_2 + \beta\text{-FeOOH} \rightarrow NiFe_2O_4 + H_2O(\text{hydrothermal})$$

3.2. Characterization

Phase investigations of the products were performed by X-ray diffraction (XRD). The XRD curves of the optimum Pd-$NiFe_2O_4$/rGO-4 photocatalyst and the counterparts of pure $NiFe_2O_4$ and the optimum $NiFe_2O_4$/rGO-4 photocatalyst are presented in Fig. 1a. The peaks at the 2θ values of 18.3°, 30.1°, 35.3°, 43.0°, 53.5°, 56.3° and 62.4° are assigned to the (1 1 1), (2 2 0), (3 1 1), (4 0 0), (4 2 2), (5 1 1) and (4 0 0) crystal planes of $NiFe_2O_4$ (JCPDS card no. 22-1086) [32], respectively. As to the sample of Pd-$NiFe_2O_4$/rGO-4 nanocomposite, peaks at 39.6° and 45.4° can be well-indexed as the (1 1 1), (2 0 0) diffractions of crystalline Pd (JCPDS card no. 46-1043) [32], which indicates the presence of Pd nanoparticles. The main XRD peaks of $NiFe_2O_4$/rGO-1, $NiFe_2O_4$/rGO-2, $NiFe_2O_4$/rGO-3 and $NiFe_2O_4$/rGO-5 nanocomposites are similar to $NiFe_2O_4$/rGO-4 nanocomposite (Fig.S1); all the peaks correspond to the cubic spinel $NiFe_2O_4$. The main XRD peaks of Pd-$NiFe_2O_4$/rGO-1, Pd-$NiFe_2O_4$/rGO-2, Pd-$NiFe_2O_4$/rGO-3 and Pd-$NiFe_2O_4$/rGO-5 nanocomposites are similar to Pd-$NiFe_2O_4$/rGO-4 nanocomposite (Fig. S2), which indicates the introduction of rGO and Pd nanoparticles do not generate the new phase of $NiFe_2O_4$. Meanwhile, all peaks of XRD patterns are narrow because of high crystallinity [36], while no impurities peaks are detected.

FT-IR spectroscopy was applied to certify the reduction process of GO. In Fig. 1b, the absorption peaks at 3420, 1730, 1620, 1225 and 1068 cm^{-1} are observed in the FT-IR spectrum of GO, which belong to the stretching vibrations of O—H, C=O in the carboxyl group, C=C in the aromatic ring, C—OH and epoxy C— O—C, respectively [32]. However, the oxygen functional group peaks at 1730 and 1068 cm^{-1} almost disappeared in the FT-IR spectra of the $NiFe_2O_4$/rGO-4 and Pd-$NiFe_2O_4$/rGO-4 nanocomposites, indicating the efficient reduction of GO to rGO by ethanol during the hydrothermal process [32]. All the FT-IR spectra of the $NiFe_2O_4$, $NiFe_2O_4$/rGO-4 and Pd-$NiFe_2O_4$/rGO-4 nanocomposites exhibit a characteristic absorption peak at 590 cm^{-1}, which is the inherent stretching vibrations of Fe—O bond in $NiFe_2O_4$ [32].

Raman spectroscopy, a powerful tool for studying oxides structure and the structural changes of carbonaceous materials [37], was employed to analyze the vibrational properties of as-prepared nanocomposites (Fig. 1c). The Raman peaks at 475 and 685 cm^{-1} of $NiFe_2O_4$ are assigned to $T_{2g(2)}$ and A_g vibration modes, which are well correspond with the reported results of $NiFe_2O_4$ crystalline [32]. In the Raman spectrum of GO, the D peak at 1360 cm^{-1} is derived from the defective structures of carbon material, while the G peak at 1602 cm^{-1} is related to E_{2g} graphite mode, reflecting the graphitization of carbon material [37]. The intensity ratio of D peaks to G peaks (I_D/I_G) reflects the structure quality and the defective extent of GR [37]. Generally, the greater the I_D/I_G, the poorer the graphite structure of carbon material consists. After the hydrothermal reduction, the I_D/I_G intensity ratio of $NiFe_2O_4$/rGO-4 (1.15) and Pd-$NiFe_2O_4$/rGO-4 nanocomposites (1.25) are higher than that of the GO (0.95). This change suggests a decrease in size of the sp^2 domains after the reduction of GO, because the smaller sizes graphitic domains are created [37]. However, the unrepaired defects can retained after the removal of the majority of oxygen-containing functional groups, which can lead to the increase of I_D/I_G intensity ratios [37]. In addition, the unrepaired defects also can make the G and D band of $NiFe_2O_4$/rGO-4 and Pd-$NiFe_2O_4$/rGO-4 nanocomposites shifted to lower frequency as compared with that of GO [37]. Thus, the Raman spectra can illustrate that GO was reduced to rGO, which is in accordance with that of FT-IR spectroscopy analysis.

The magnetic performances of the as-synthesized nanocomposites were measured with a vibrating sample magnetometer at room temperature. As shown in Fig. 1d, the saturation magnetization of $NiFe_2O_4$, $NiFe_2O_4$/rGO-4 and Pd-$NiFe_2O_4$/rGO-4 are 57.5, 28.6 and 27.8 emu/g, respectively. Generally, saturation magnetization of magnetic nanoparticles is mainly dependent on their particle size, the magnetization decreased as the magnetic particle size decreased [32]. Thus, the decreased value of saturation magnetization can be mainly attributed to the smaller size of $NiFe_2O_4$ on the surface of rGO than that of pure $NiFe_2O_4$ particles. In addition, the magnetization intensities of Pd-$NiFe_2O_4$/rGO-4 nanocomposite is a little lower than that of the $NiFe_2O_4$/rGO-4, which is mostly because of the Pd nanoparticles loading on the surface of $NiFe_2O_4$ nanoparticles [32]. Thus, the Pd-$NiFe_2O_4$/rGO-4 nanocomposite

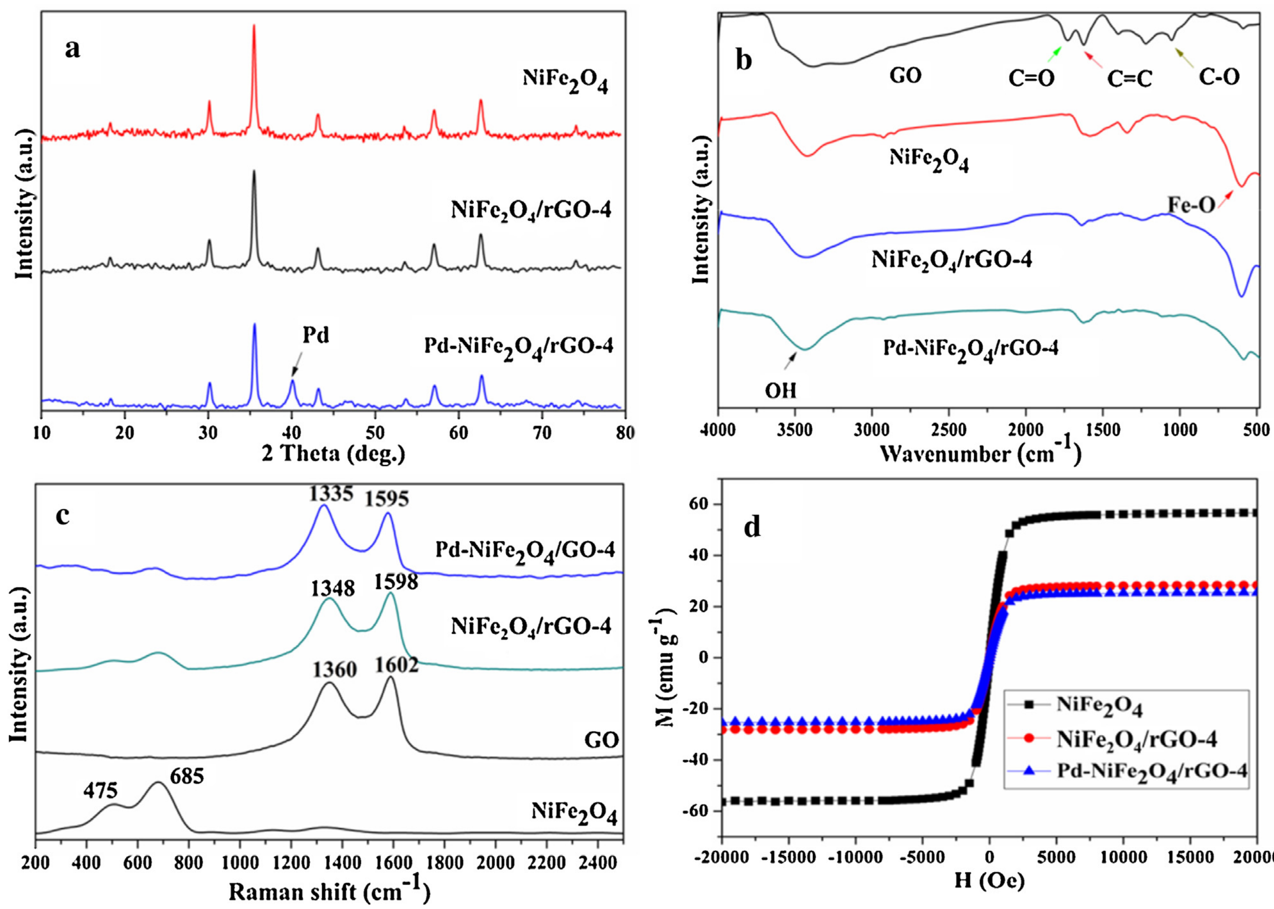

Fig. 1. (a) XRD; (b) FT-IR; (c) Raman spectra; (d) Magnetization curves at 300 K.

can be readily separated from the reaction system with an external magnetic field.

X-ray photoelectron spectroscopy (XPS) is a useful tool to analyze the chemical composition of material. Fig. 2a presents the C 1s XPS spectrum of GO, it can de-convoluted into three distinct peaks at 284.6 eV for C—C/C=C, 286.5 eV for C—OH and 287.9 eV for O=C—OH, respectively [38]. Fig. 2b is the wide scan XPS spectrum of Pd-$NiFe_2O_4$/rGO-4 nanocomposite, which reveals the signals for C, O, Fe, Ni and Pd elements. We de-convoluted the C 1s XPS spectrum of Pd-$NiFe_2O_4$/rGO-4 nanocomposite into two peaks of C—C (284.8 eV) and C—OH (286.0 eV) (Fig. 2c). The peak of C—OH is very small, indicating that GO has been effectively reduced to rGO [38], which is in agreement with the FT-IR and Raman results. In the high resolution XPS spectrum of Pd 3d peaks (Fig. 2d), the binding energies present at 335.4 and 340.7 eV belong to Pd $3d_{3/2}$ and Pd $3d_{5/2}$, respectively [32], with a spin-orbit gap of 5.3 eV, indicating the existence of metallic Pd rather than Pd^{2+}. The XPS spectrum of Ni 2p (Fig. 2e) suit well to two peaks at 855.5 eV and 862.3 eV, readily belonged to the Ni $2p_{3/2}$ and Ni $2p_{1/2}$, respectively [32]. Two XPS peaks located at 711.2 and 725.0 eV are binding energies of Fe $2p_{3/2}$ and Fe $2p_{1/2}$ (Fig. 2f) [32]. After further analysis of O 1s (Fig. S3), the peak located at 532.0 eV in the O 1s is the residual oxygen containing groups, such as −OH and −COOH, which bonded with C atoms of rGO sheets [39]. Significantly, we found a conspicuous 530.9 eV peak, which belong to the O—$NiFe_2O_4$ interfacial bonding structure, it suggest that the $NiFe_2O_4$ and the residue oxygen of rGO have bonding effect [40]. Another peak at 530.0 eV is the signal of O 1s in $NiFe_2O_4$ [41].

The morphologies of Pd-$NiFe_2O_4$/rGO-4 nanocomposite were characterized by SEM, EDX-mapping, TEM and HR-TEM. Fig. 3a and 3b illustrates the SEM images of Pd-$NiFe_2O_4$/rGO-4 nanocomposite. From the images of Fig. 3a, we can see that rGO nanosheets show curled and corrugated with a paper-like morphology. Nanoparticles are uniformly dispersed on the surface of rGO nanosheets in Fig. 3b. Fig. S4 shows the EDX spectrum of Pd-$NiFe_2O_4$/rGO-4 nanocomposite, it reveal that the elements C, O, Fe, Ni, and Pd present in the Pd-$NiFe_2O_4$/rGO-4 nanocomposite. The EDX-mapping (Fig. 3c–g) in the yellow frame of Fig. 3a indicates that all the elements have a uniform dispersity on the plane of rGO. The TEM image of Fig. 3i indicate that the Pd and $NiFe_2O_4$ nanoparticles are loaded on the rGO sheets. It can be seen from Fig. 3h that the size of the Pd nanoparticles are mainly distributed in 8–12 nm. In the images of Fig. 3j, clear lattice fringes are observed. The crystal lattice fringes of the spacing of 0.23 nm and 0.29 nm are assigned to the (1 1 1) plane of Pd and the (3 1 1) plane of $NiFe_2O_4$, respectively, which are in accordance with the XRD data [42].

All the above analyses accounted for the successful preparation of Pd-$NiFe_2O_4$/rGO nanocomposites.

In the photocatalytic process, optical absorption performance of photocatalysts is very important. Fig. S5 displays the UV–vis diffuse reflectance spectra (DRS) of pure $NiFe_2O_4$, $NiFe_2O_4$/rGO-4 and Pd-$NiFe_2O_4$/rGO nanocomposites. As shown in Fig. S5, there is a gradually enhanced visible light absorption of $NiFe_2O_4$/rGO-4 and Pd-$NiFe_2O_4$/rGO nanocomposites with the increasing content of rGO, as compared to pure $NiFe_2O_4$. This can be attributed to the inherent absorption of black colored rGO and the electronic transition between rGO and $NiFe_2O_4$ [43]. Such phenomenon was also observed in other binary $NiFe_2O_4$/rGO nanocomposites, therefore, the introduction of rGO to $NiFe_2O_4$ system can lead to a bridge between the incident light and $NiFe_2O_4$, and triggering

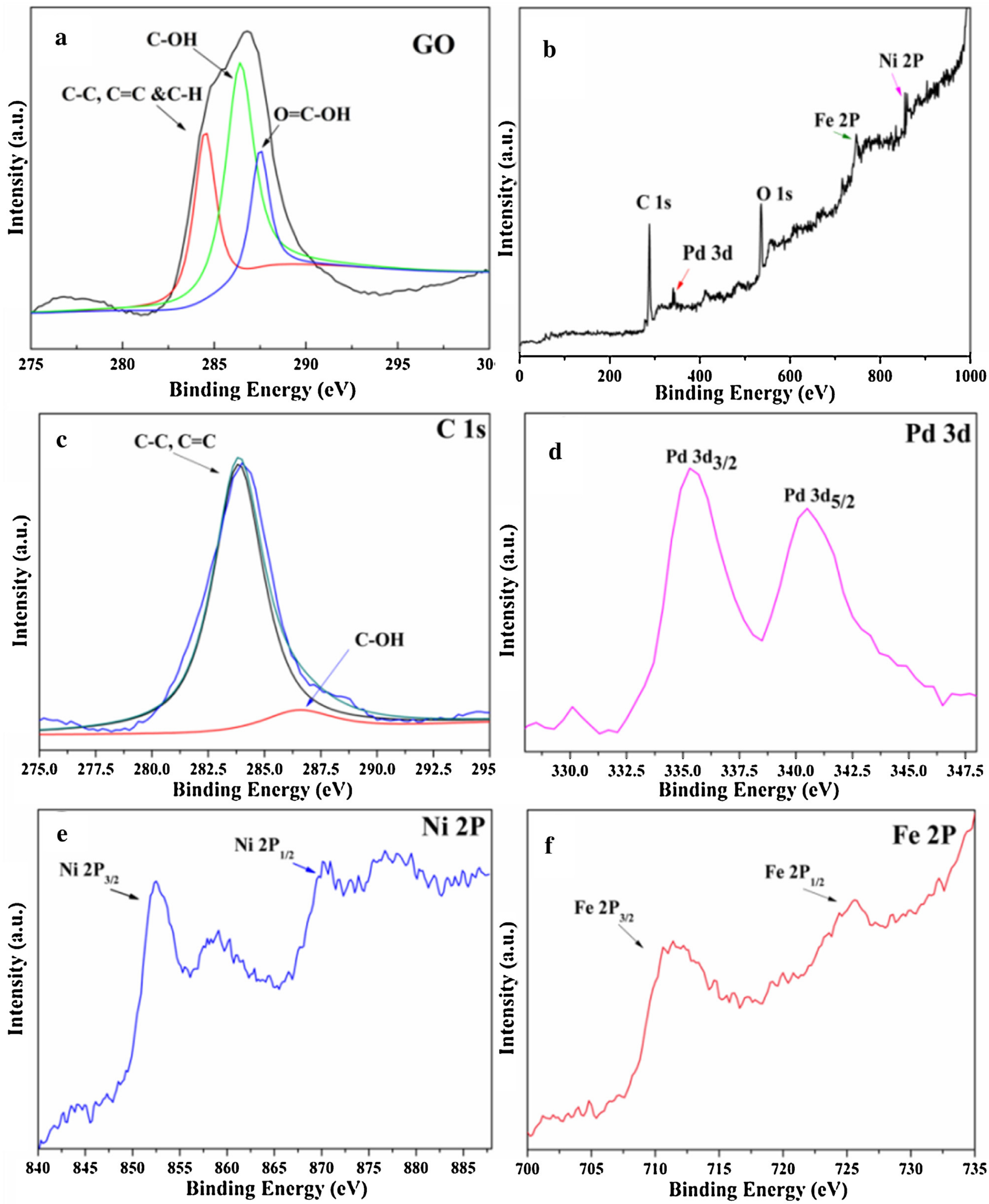

Fig. 2. (a) high-resolution XPS spectra of C1s peaks of GO; (b) wide scan XPS spectra of Pd-$NiFe_2O_4$/rGO-4; (c) high-resolution XPS spectra of C1s peaks, (d) Pd 3d peaks, (e) Ni 2p peaks and (f) Fe 2p peaks in Pd-$NiFe_2O_4$/rGO-4 nanocomposite.

a photocatalytic process [19]. The DRS tests also demonstrated that Pd nanoparticles do not change the optical properties of Pd-$NiFe_2O_4$/rGO nanocomposites, as compared to the counterparts of $NiFe_2O_4$/rGO. In other words, the interfacial contact, morphology and crystalline phase of $NiFe_2O_4$/rGO can be retained in the ternary Pd-$NiFe_2O_4$/rGO nanocomposites regardless of Pd nanoparticles. Therefore, Pd-$NiFe_2O_4$/rGO nanocomposites provide a reasonable platform to investigate the “interfacial mediator” role of Pd nanoparticles.

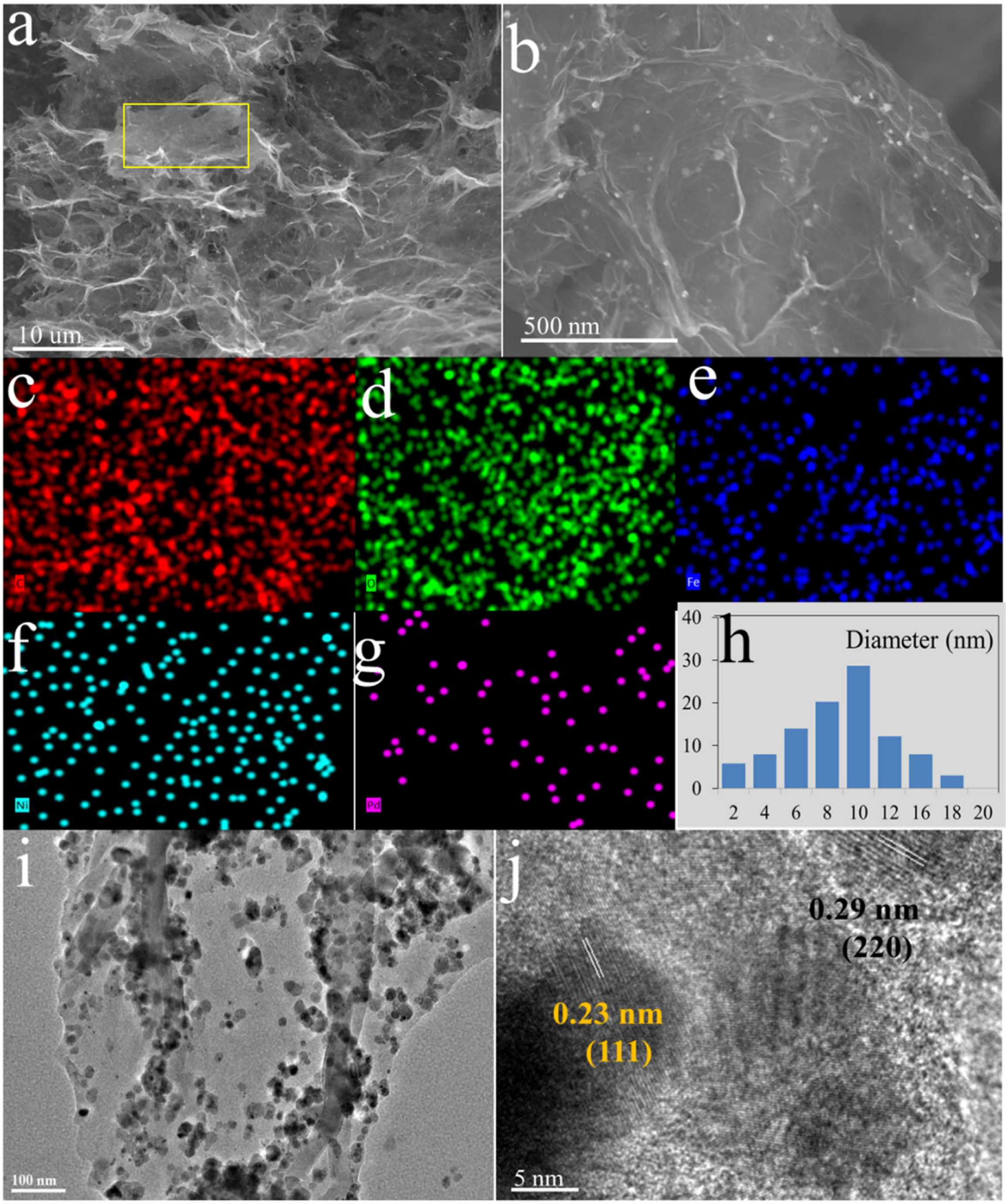

Fig. 3. (a) and (b) SEM images of Pd-$NiFe_2O_4$/rGO-4 nanocomposite; EDX-mapping of C (c), O (d), Fe (e), Ni (f), and Pd (g) of Pd-$NiFe_2O_4$/rGO-4 nanocomposite in the yellow frame of (a); (h) size distribution of the Pd NPs; (i) TEM image, and (j) HR-TEM image of Pd-$NiFe_2O_4$/rGO-4 nanocomposite. (For interpretation of the references to color in this figure legend, the reader is referred to the web version of this article.).

3.3. Photocatalytic activity properties

Visible light degradation of organic dyes has been widely used as a hopeful strategy for environmental remediation. In this work, a probe molecule of Rodamine-B (RhB) was chosen as the model organic dye. Fig. 4a shows the photocatalytic activity of bare $NiFe_2O_4$ and $NiFe_2O_4$/rGO nanocomposites with different amount of rGO for the degradation of RhB solution. Fig. 4a-(1) shows that the concentration did not change under the visible light irradiation without any photocatalyst. After added the bare $NiFe_2O_4$ powder, about 18.5% RhB solution was removed after 4 h irradiation (Fig. 4a-(3)), which is higher than the identical measurement under the dark (Fig. 4a-(2)). In the $NiFe_2O_4$/rGO nanocomposites, the $NiFe_2O_4$/rGO-4 demonstrates the best photocatalytic performance (Fig. 4a-(9)). After adsorption and visible light illumination, the decolorization percentage of RhB solution is about 89.5% after 4 h, and the pure adsorption capacity of $NiFe_2O_4$/rGO-4 under dark is around 20.5% (Fig. 4a-(4)). It illustrates that rGO played a key role in improving the photocatalytic activity of $NiFe_2O_4$. When comparing the curve (5), (6), (7), (8) and (9) in Fig. 4a, we can see that the photocatalytic activity of the $NiFe_2O_4$/rGO nanocomposites first increased,

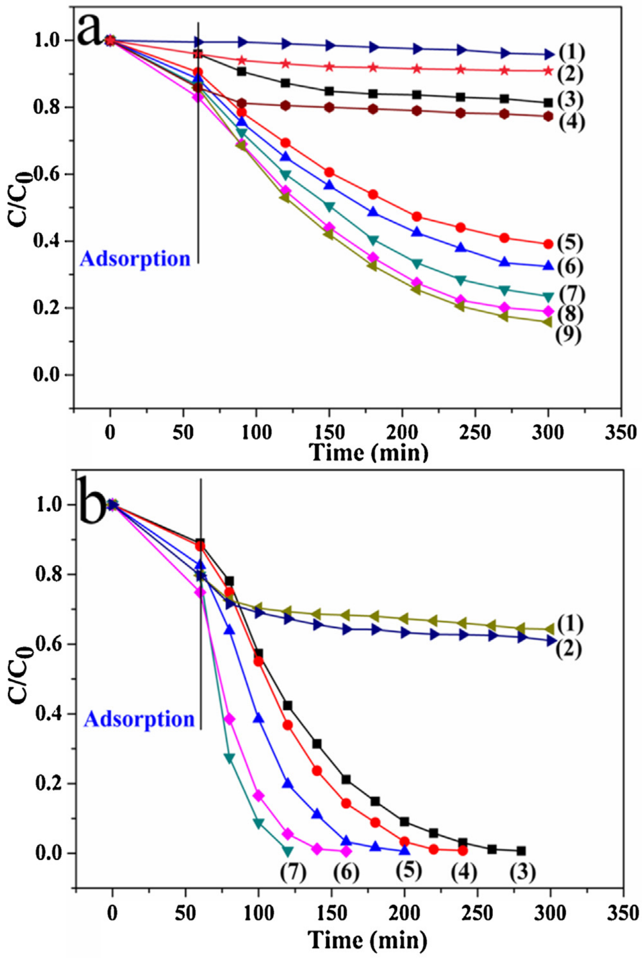

Fig. 4. Visible light degradation of RhB solution, (a)-(1) No catalyst; (a)-(2) $NiFe_2O_4$ (dark); (a)-(3) $NiFe_2O_4$; (a)-(4) $NiFe_2O_4$/rGO-4 (dark); (a)-(5) $NiFe_2O_4$/rGO-1; (a)-(6) $NiFe_2O_4$/rGO-2; (a)-(7) $NiFe_2O_4$/rGO-3; (a)-(8) $NiFe_2O_4$/rGO-5; (a)-(9) $NiFe_2O_4$/rGO-4; (b)-(1) Pd-$NiFe_2O_4$/rGO-4 (dark); (b)-(2) Pd-/rGO; (b)-(3) Pd-$NiFe_2O_4$/rGO-1; (b)-(4) Pd-$NiFe_2O_4$/rGO-2; (b)-(5) Pd-$NiFe_2O_4$/rGO-3; (b)-(6) Pd-$NiFe_2O_4$/rGO-5; (b)-(7) Pd-$NiFe_2O_4$/rGO-4;.

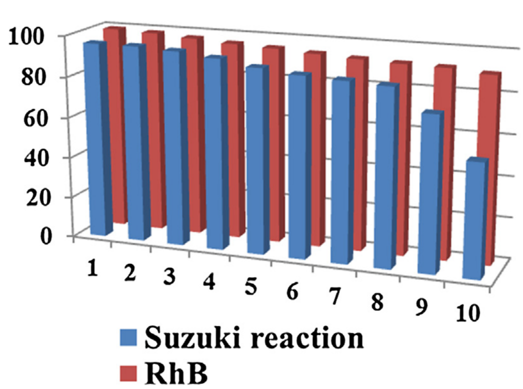

Fig. 5. The reusability of the Pd-$NiFe_2O_4$/rGO-4 photocatalyst for the photodegradation of RhB solution and the benchmark reaction of Suzuki–Miyaura coupling reaction.

and then decreased with the increasing amount of rGO. The reasons may be that rGO nanosheets worked as an electron acceptor can readily transfer the photogenerated electrons from $NiFe_2O_4$ under irradiation, restraining the recombination rate of photogenerated electron-hole pairs and thus improving the photocatalytic dye degradation activity of $NiFe_2O_4$ [44]. The decreased

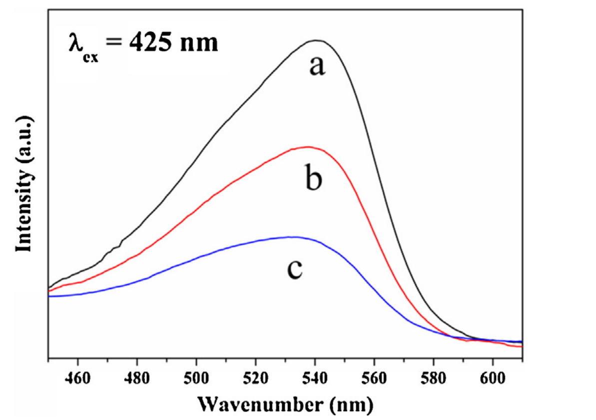

Fig. 6. PL spectra of (a) pure $NiFe_2O_4$, (b) $NiFe_2O_4$/rGO-4, (c) Pd-$NiFe_2O_4$/rGO-4 upon 425 nm excitation.

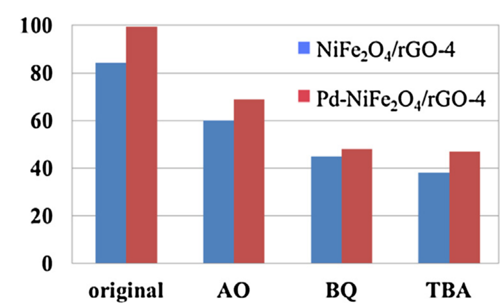

Fig. 7. Control experiments with different radical scavengers for the photocatalytic RhB degradation (20 mg/mL) over $NiFe_2O_4$/rGO-4 and Pd-$NiFe_2O_4$/rGO-4 under visible light irradiation for 4 h and 1 h, respectively.

activity can be considered to the increased dyes absorption capacity, scattering of photons by rGO and the reduced light absorption of $NiFe_2O_4$ [45]. The similar phenomenon appears in most of the binary graphene-based photoreaction systems, which is so-called as the “shielding effect” of graphene [46]. Thus, the addition amount ratio of rGO in the rGO-based photocatalysts is generally appropriate or lower to keep a desirable balance between the two-edged effects of rGO.

Fig. 4b is the photocatalytic activity of ternary Pd-$NiFe_2O_4$/rGO nanocomposites. It can be seen from Fig. 4b, when a little amount of Pd is added, the degradation rate of RhB solution is significantly enhanced. For example, the degradation rate increases from 89.5% over $NiFe_2O_4$/rGO-4 to 98.6% for Pd-$NiFe_2O_4$/rGO-1 with 4 h visible light illumination (Fig. 4b-(3)). For the ternary Pd-$NiFe_2O_4$/rGO nanocomposites, Pd-$NiFe_2O_4$/rGO-4 (70 mg GO) exhibits the optimum photocatalytic activity with the degradation rate as high as ca. 99.5% by 1 h irradiation (Fig. 4b-(7)), which is higher than that of the blank-$NiFe_2O_4$ (18.5%, 4 h) and $NiFe_2O_4$/rGO (89.5%, 4 h). Moreover, the pure adsorption capacity of Pd-$NiFe_2O_4$/rGO-4 under dark is also higher than the $NiFe_2O_4$/rGO-4, which exhibit about 31.2% adsorption after 4 h (Fig. 4b-(1)). The interesting result conveys the crucial information about the “shielding effect”, which can result in blocking of incident light absorption by the photocatalysts [47]. For this matter, in this case, the negative “shielding effect” of rGO can be counterbalanced in the Pd-$NiFe_2O_4$/rGO nanocomposites to a great extent by the Pd nanoparticles. However, further increasing rGO in the Pd-$NiFe_2O_4$/rGO-5 nanocomposites, leads to a deterioration of the photocatalytic activity. It can be attributed to the higher amount of rGO have increased “shielding effect” and stronger dyes adsorption capacity, meanwhile, $NiFe_2O_4$ ingredient will be decreased.

To investigate the possible role of Pd nanoparticles, we prepared the Pd/rGO nanocomposite and evaluated its photocatalytic

activity. The result shows that Pd/rGO exhibits low photoactivity (Fig. 4b-(2)), indicating that the enhanced photocatalytic activity of Pd-$NiFe_2O_4$/rGO cannot be attributed to the intrinsic catalytic activity of Pd nanoparticles. In other words, Pd nanoparticles only play a co-catalyst role in the photocatalytic RhB degradation. Fig. S6 is the absorption spectra of RhB solution and revealed the photodegradation process by the Pd-$NiFe_2O_4$/rGO-4 nanocomposite. Further studies show that the Pd-$NiFe_2O_4$/rGO-4 photocatalyst can degrade methyl orange (MO) and methyl blue (MB) under visible light irradiation, Fig. S7 and Fig. S8 show the photodegradation process of MO and MB. It indicates that Pd-$NiFe_2O_4$/rGO enable photodegradation of multiple organic dyes under visible light irradiation.

In order to compare the degradation effect of Pd-$NiFe_2O_4$/rGO-4 and that of the developed photocatalyst, especially graphene-semiconductor photocatalysts (Table S1), involved noble metal ternary or quaternary rGO-based photocatalysts (Table S2), graphene-MFe_2O_4 photocatalysts (Table S3). Although some of the catalytic efficiency is better than our catalyst, we still think that our photocatalyst is an outstanding catalyst in the photocatalytic dyes degradation. Significantly, the recyclability for the photocatalytic dyes degradation of Pd-$NiFe_2O_4$/rGO-4 is the best in all the provided results. We also tested the visible light degradation of 50 and 100 mg/L RhB solution by the Pd-$NiFe_2O_4$/rGO-4 photocatalyst, which exhibit about 99.1% and 98.5% degradation after 2 h and 4 h, respectively (Fig. S9)

Recently, light-catalyzed chemical reactions have aroused much attention due to the green and environmentally benign synthetic process [34,48]. Pd is well-known to be a catalytically active species for many important chemical reactions [49]. However, most of organic reactions are carried out under the heating condition, which is energy intensive. Thus, it will be a remarkable breakthrough if we can improve the catalytic activity of Pd catalyst at ambient temperatures depending visible light, the abundant, reliable, and green energy source [50].

Therefore, we investigate the photocatalytic chemical reaction of Pd-$NiFe_2O_4$/rGO using the Suzuki–Miyaura coupling reaction of 4-iodoanisole and phenylboronic acid as the benchmark reaction. In consideration of the fact that photothermal effect can conduce to the conversion of chemical reaction in principle [51], the temperature was maintained at 25 °C with a water bath. As shown in Table S4, Pd-$NiFe_2O_4$/rGO-4 gives an excellent yield (90%) under visible light irradiation for 1 h (entry 1). It clearly demonstrated that visible light can smoothly operate the Suzuki coupling reaction under ambient temperatures. For comparison, we conducted the same reaction without visible light irradiations under the same conditions. Unfortunately, only a yield of 12% was obtained (Table S4, entry 2). Moreover, no product was gained with either $NiFe_2O_4$ (Table S4, entry 3) or $NiFe_2O_4$/rGO-4 (Table S4, entry 4), and low yield with Pd/rGO (Table S4, entry 5), which confirmed the importance of combining the $NiFe_2O_4$ photocatalyst with Pd nanoparticles to carry out the Suzuki coupling reaction. To reveal the structural advantage of the Pd-$NiFe_2O_4$/rGO, we also use the Pd-$NiFe_2O_4$ as the photocatalyst for a comparison, while only a yield of 55% is obtained (Table S4, entry 6). Then, we carried out the benchmark reaction under visible light irradiation at 25 °C for 0.5 h, and keep in the dark for 0.5 h, the yield is 72% (Table S4, entry 7). This result indicates that visible light is indeed the motive power in this chemical conversion system [52]. We also tested the photocatalytic activities of Pd-$NiFe_2O_4$/rGO-1, Pd-$NiFe_2O_4$/rGO-2, Pd-$NiFe_2O_4$/rGO-3 and Pd-$NiFe_2O_4$/rGO-5. However, all the yields are lower than that of Pd-$NiFe_2O_4$/rGO-4 (Table S4, entry 8–11).

Generally, rGO can adsorb the organic molecules and improve the photocatalytic activity of rGO-based photocatalysts [53]. What's more, the synergistic effects of bonding $NiFe_2O_4$ and rGO make the photoelectrons transfer from $NiFe_2O_4$ to rGO, which can restrain the electron-hole recombination. Simultaneously, Pd nanoparticles act as the "intermediator" roles on the interfacial matrix between $NiFe_2O_4$ and rGO. The Pd nanoparticles also can be used as "electron reservoir" to delay the recombination of photogenerated electron-hole pairs of $NiFe_2O_4$. Such a sample "intermediator" role and "electron reservoir" strategy thus lead to the enhancing photocatalytic performance of the Pd-$NiFe_2O_4$/rGO.

Then, we tested the light-catalyzed Suzuki coupling reactions with various substituted aryl halides and arylboronic acids, the reactions were also tested under the 80 °C condition as comparison. It is well known that the conversion of the Suzuki coupling reactions rely on the halogen element (I, Br, Cl), the positions of the substituent groups and their withdrawing-electron or donating-electron capabilities [54]. We can see from Table 1, when halogen element is I, the reaction can be completed within 0.5 h with yields of 99% (Table 1, entries 1). Iodobenzenes with electron-donating groups (NH_2, and OCH_3) and electron-withdraw groups (CH_3CO) were selected to investigate the electronic effect on the photocatalytic performance. It can be observed that the electron-donating groups (Table 1, entries 2, 5) have negative effect on the yields of the coupled products as comparison to the electron-withdraw groups (Table 1, entries 3). The steric hindrance also has negative effect (Table 1, entries 4). For the bromobenzene or substituent groups bromobenzenes, the coupling reactions can also be completed well with excellent yields after prolong the time (Table 1, entries 6–8). The substituted arylboronic acid also underwent the coupling reaction with iodobenzene with our photocatalytic system (Table 1, entries 9–12). Interestingly, both electron-withdrawing (F) and electron-donating (CH_3, OCH_3) groups arylboronic acid do not have an inhibition effect with the same conditions (Table 1, entries 9, 11, 12). The *ortho*-methyl phenylboronic acid gives a lower yield (Table 1, entries 10) can be attribute to the steric hindrance. However, the activity of chlorobenzene is poor in the same process and providing a medium yields even prolong the time to six hours (Table 1, entries 13–14).

The yields of thermocatalytic Suzuki–Miyaura coupling reactions also present in Table 1. After comparing the yields of photocatalytic and thermocatalytic Suzuki coupling reactions, we can drew the conclusion that the photocatalytic Suzuki reaction can completely replace the thermocatalytic Suzuki reaction to carry out the reaction under room temperature. For comparing the photocatalytic performances of different photocatalyst systems for Suzuki reactions, we collect the typical results from the literature. As shown in Table S5, most of these photocatalytic systems give rise to excellent yields with low temperature under different light source. Nevertheless, even though some of them gained the high yields, toxic solvents (such as DMF), phase transfer reagent (such as CTAB) and strong light energy are used or the reaction needs a long time to occur. Significantly, the recyclability of our photocatalyst is the best in all the provided results.

Except the outstanding multifunctional photocatalytic activity, isolation and reusability of the photocatalyst is very important for any practical application [55]. In this work, the Pd-$NiFe_2O_4$/rGO can be easily isolated due to the inherent magnetism of $NiFe_2O_4$. Both the photodegradation of RhB solution and the benchmark reaction of Suzuki–Miyaura coupling reaction are selected to survey the reusability of Pd-$NiFe_2O_4$/rGO. As illustrated in Fig. 5, the photocatalyst Pd-$NiFe_2O_4$/rGO-4 can be reused ten times for the photodegradation of RhB solution without an obvious decrease and eight times for the Suzuki–Miyaura coupling reaction with a yield higher than 85%. The reason of the decreased catalyst activity for the Suzuki reaction may be associated with the catalyst reaction mechanism. The Suzuki reactions need Pd nanoparticles to initiate the oxidation addition reaction. Due to the high surface energies, Pd nanoparticles tend to leaching during catalytic reactions, and leading to a reduced catalytic activity [56]. On the other hand, the

Table 1
photocatalytic or thermocatalytic Suzuki–Miyaura coupling reactions by Pd-$NiFe_2O_4$/rGO-4.

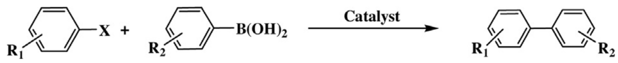

Entry[a]	Aryl halides	Arylboronic acids	Time/h	Yield[b]	Yield[c]
1	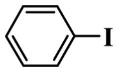	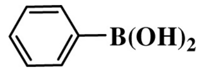	0.5	>99	>99
2	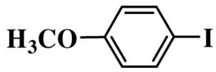	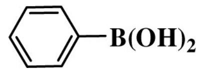	1	90	92
3	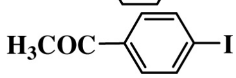	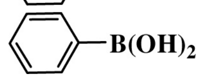	1	97	96
4	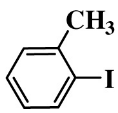	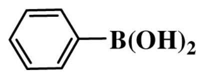	1	82	84
5	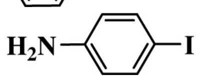	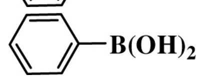	1	80	83
6	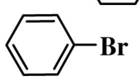	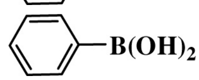	1.5	98	97
7	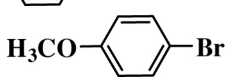	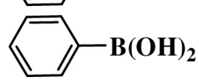	1.5	89	90
8	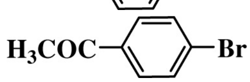	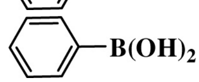	1.5	94	94
9	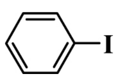	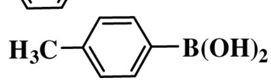	1	95	94
10	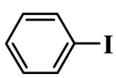	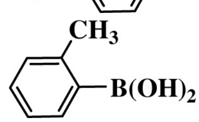	1	81	83
11	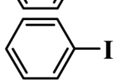	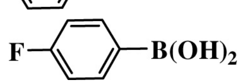	1	97	98
12	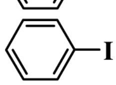	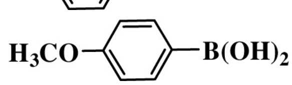	1	96	94
13	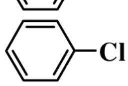	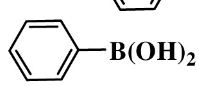	2	25	33
14	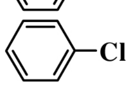	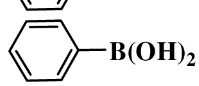	6	55	60

Reaction conditions.
[a] Aryl halide (1.0 mmol), arylboronic acid (1.2 mmol), potassium carbonate (2.5 mmol), 5 mL ethanol-water (9:1), N_2 atmosphere, catalyst (0.5 mmol% Pd), GC yields.
[b] Visible light irradiation.
[c] At 80 °C.

soluble leaching Pd can nucleate to form Pd clusters also resulting in the decreased activity [57]. Fig. S10 and Fig. S11 show the XRD and TEM images of Pd-$NiFe_2O_4$/rGO-4 after ten times of recycling experiments. All the XRD peaks of the used Pd-$NiFe_2O_4$/rGO-4 can be corresponded to the cubic spinel $NiFe_2O_4$, and no impurities peaks are detected. Unsatisfactorily, the TEM images indicate that parts of nanoparticles have reunited on the surface of rGO.

3.4. Photocatalytic mechanism

Many factors can influence the photocatalytic activity. Firstly, in order to rule out the photosensitization role of dyes during the photocatalytic reaction, we have selected phenol as a colorless contaminant to test the photocatalytic behavior of the as-prepared samples [58]. As shown in Fig. S12, after 1 h of visible light illumination, $NiFe_2O_4$, $NiFe_2O_4$/rGO-4 and Pd-$NiFe_2O_4$/rGO-4 nanocomposites exhibited degradation efficiencies of 12.8%, 40.8% and 85.3% towards the degradation of phenol solution (20 mg/L), respectively. The catalysts showed less photoactivity towards phenol degradation than those of RhB degradation. Secondly, as stated above, because of the narrow band gap of the $NiFe_2O_4$, the Pd-$NiFe_2O_4$/rGO photocatalysts are expected to obtain more efficient utilization of the visible light and thus show the enhance photocatalytic capacity [59]. Thirdly, as is well-known, a higher specific surface areas and larger pore volumes of photocatalysts are beneficial for enhancing the photocatalytic performance [60]. The surface areas of $NiFe_2O_4$, $NiFe_2O_4$/rGO-4 and Pd-$NiFe_2O_4$/rGO-4 are shown in Fig. S13, and the corresponding parameters of BET surface areas and pore volumes are listed in Table S6. Evidently, the BET surface areas of Pd-$NiFe_2O_4$/rGO-4 (24.6 $m^2\ g^{-1}$) and $NiFe_2O_4$/rGO-4 (22.8 $m^2\ g^{-1}$) are higher than that of $NiFe_2O_4$ (9.5 $m^2\ g^{-1}$). As shown in Fig. 4, the adsorption capacity of $NiFe_2O_4$, $NiFe_2O_4$/rGO-4 and Pd-$NiFe_2O_4$/rGO-4 are 7.8%, 20.5% and 31.2%, respectively. Finally, the efficient charge separation and transportation are vital in the photocatalysis process. Photoluminescence (PL) is an effective basic way to analyze the charge carrier immigration and transfer

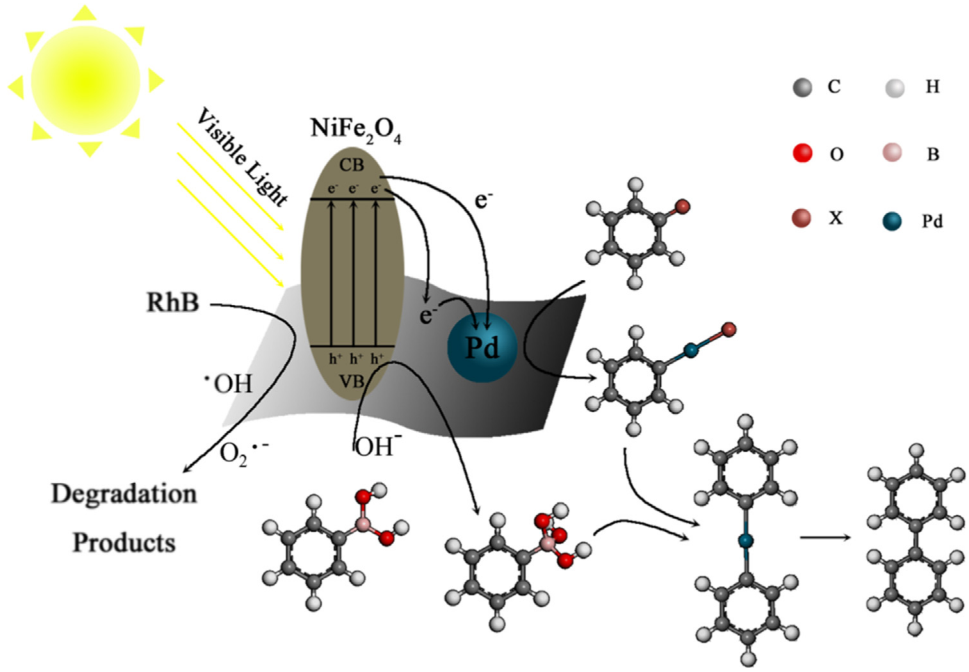

Fig. 8. The Schematic diagram of the possible photocatalytic mechanism over the Pd-NiFe$_2$O$_4$/rGO nanocomposite photocatalyst.

[61]. Generally, a lower PL intensity means a lower electron-hole recombination rate [61], which can result in a higher photocatalytic activity. Fig. 6 shows the PL spectra of NiFe$_2$O$_4$, NiFe$_2$O$_4$/rGO-4 and Pd-NiFe$_2$O$_4$/rGO-4 with an excitation wavelength of 425 nm. It is clearly observed that the pure NiFe$_2$O$_4$ present a strong PL intensity at around 540 cm^{-1}, which can be attributed to the transition from 3d^5 to 3d^3 4s of Fe^{3+} ions [62]. And the PL signal is reduced for the NiFe$_2$O$_4$/rGO-4, indicating that the recombination rate of the excitons in NiFe$_2$O$_4$ is efficiently hampered. In the case of Pd-NiFe$_2$O$_4$/rGO-4, the PL signal is further reduced, suggesting that more photogenerated electrons are trapped by Pd and rGO, thereby resulting in the obviously PL quenching [63]. It is concluded that not only rGO, but also Pd can trap the photogenerated electrons of NiFe$_2$O$_4$ to restrain the recombination of hole-electron pairs.

To investigate the possible active species in our photocatalytic dye degradation system, three controlled experiments have been performed via different radical scavengers. As shown in Fig. 7, when adding the ammonium oxalate (AO), *tert*-butyl alcohol (TBA) and benzoquinone (BQ) for photogenerated holes (h$^+$), hydroxyl radicals (•OH) and superoxide radicals (O$_2$•$^-$), respectively [64], the photocatalytic RhB solution over the NiFe$_2$O$_4$/rGO-4 and Pd-NiFe$_2$O$_4$/rGO-4 is inhibited.

Additional control experiments were also performed to investigate the role of the photogenerated e$^-$ and h$^+$ for the Suzuki coupling reaction. After the addition of e$^-$ scavenger of $K_2S_2O_8$, low yield is obtained under light irradiation (Table S4, entry 12). According to the reaction mechanism of Suzuki coupling over Pd-based catalysts, the catalytic activity will be enhanced with increasing electron density of Pd nanoparticles, which lead to a faster rate of the oxidative addition reaction [65]. Therefore, photogenerated e$^-$ transferred onto the Pd nanoparticles can enhance the inherent catalytic activity of Pd. And then, when we add the h$^+$ scavenger of AO, lower yield is gained under light irradiation (Table S4, entry 13). However, the same reaction carries out well at 80 °C without visible light irradiations in the presence of AO (Table S4, entry 14). It clearly demonstrated that the light-catalyzed Suzuki reaction rely on the photogenerated h$^+$, which can stimulate the C-B bonds of the arylboronic acids [66]. Without N_2 atmosphere, the yield of the coupling product decreased to 82% (Table S4, entry 15). This is due to the O$_2$•$^-$, which produced by the photogenerated e$^-$ and dissolved oxygen, can break down the adsorbed molecules and form the undesired by-products [67]. What is more, the consumption of the photogenerated e$^-$ by dissolved oxygen is distasteful for enhancing the electron density of Pd [67].

Based on the above controlled experimental results and discussions, it can be deduced that the successful photocatalytic dyes degradation are mainly driven by the adsorption property and the participation of photogenerated h$^+$, •OH and O$_2$•$^-$ radicals. A possible mechanism for the photocatalytic dyes degradation is summarized in Fig. 8. Firstly, dyes molecules are partly adsorbed on the surface of Pd-NiFe$_2$O$_4$/rGO nanocomposites. Secondly, the e$^-$ is excited under the simulated visible light irradiation from the valence band (VB) to the conduction band (CB) in NiFe$_2$O$_4$, simultaneously, produced the photogenerated h$^+$ in the VB of NiFe$_2$O$_4$. The photogenerated e$^-$ may quickly transfer into the surface of rGO and the Pd surface and thus greatly reduce the recombination rate of e$^-$/h$^+$. Following, the migrated e$^-$ reacts with the dissolved O_2 to yield O$_2$•$^-$. And the corresponding h$^+$ in the VB may directly participate the photocatalytic degradation of dyes or react with H_2O to produce •OH radicals. Finally, all the produced active species of •OH, e$^-$/h$^+$ and O$_2$•$^-$ can attack the dyes molecules.

Although a more precise photoinduced mechanism for the Suzuki reaction is ambiguous, we propose a plausible mechanism on the basis of the above results and previous reports. As displayed in Fig. 8, Pd nanoparticles can trap the photogenerated e$^-$ due to its electron reservoir capacity. Both the photogenerated e$^-$ and energetic Pd nanoparticles can act as active centers to attack the C-X bond of aryl halide. Moreover, Xiao [68] et al. have proved that the C-I bond extended from 0.214 to 0.300 nm due to a photogenerated e$^-$ enters the unoccupied orbital of the iodobenzene molecule, resulting in facilitating the formation of oxidative addition intermediate with Pd. On the other hand, arylboronic acid can acquire an OH$^-$ in the basic reaction medium to form negative $B(OH)_3^-$ species, which is contribute to the *trans*-metalation process. Significantly, the h$^+$ can assist in cleaving the C-B bond to produce

biaryl-Pd complex. The remaining step, which is called the reductive elimination, should not be affected by the visible light [69].

4. Conclusions

By controlling the amount of GO, magnetically recyclable Pd-$NiFe_2O_4$/rGO nanocomposites have been successfully prepared by a one-step green hydrothermal method. The Pd-$NiFe_2O_4$/rGO illustrates enhanced photocatalytic dyes degradation activity compared with bare $NiFe_2O_4$ and optimum $NiFe_2O_4$/rGO. In addition, Pd-$NiFe_2O_4$/rGO show the effective photocatalytic Suzuki–Miyaura coupling reaction, which can completely replace the thermocatalytic Suzuki reaction under room temperature. Both the enhanced photocatalytic activities are ascribed to the efficient electron spatial transfer route due to the Pd nanoparticles, which not only act as the electron mediator on the interfacial layer of rGO and $NiFe_2O_4$, but also act as the electron reservoir to directly trap photogenerated e^-. Moreover, the Pd-$NiFe_2O_4$/rGO can be conveniently recovered using an external magnet and show excellent reusability for both the photocatalytic dyes degradation and photocatalytic chemical reaction. In summary, this work highlights the prospective and practicable of using noble metal to enhance the photocatalytic activity of rGO-based photocatalysts. On the other hand, it also advances the designing idea of more efficient rGO-based photocatalysts with the advantages of rapid recovery in multifunctional photocatalytic applications.

Appendix A. Supplementary data

Supplementary data associated with this article can be found, in the online version, at http://dx.doi.org/10.1016/j.apcatb.2016.02.054.

References

[1] S. Linic, P. Christopher, D.B. Ingram, Nat. Mater. 10 (2011) 911–921.
[2] J. Schneider, M. Matsuoka, M. Takeuchi, J.L. Zhang, D.W. Bahnemann, Chem. Rev. 114 (2014) 9919–9986.
[3] F.X. Xiao, ACS Appl. Mater. Interfaces 4 (2012) 7055–7063.
[4] S. Thangavel, M. Elayaperumal, G. Venugopal, Mater. Express 2 (2012) 327–334.
[5] M.Y. Wang, W. Zhu, D.E. Zhang, S.A. Li, W.X. Ma, Z.W. Tong, J. Chen, Mater. Lett. 137 (2014) 229–232.
[6] A.H. Ye, W.Q. Fan, Q.H. Zhang, W.P. Deng, Y. Wang, Catal. Sci. Technol. 2 (2012) 969–978.
[7] J.T. Zhang, Z.G. Xiong, X.S. Zhao, J. Mater. Chem. 21 (2011) 3634–3640.
[8] Y. Zhang, J. Tian, H. Li, L. Wang, X. Qin, A.M. Asiri, A.O. Al-Youbi, X. Sun, Langmuir 28 (2012) 12893–12900.
[9] A. Kudo, Y. Miseki, Chem. Soc. Rev. 38 (2009) 253–278.
[10] N. Gao, X. Fang, Chem. Rev. 115 (2015) 8294–8343.
[11] H.F. Liu, Z.G. Jia, S.F. Ji, Y.Y. Zheng, M. Li, H. Yang, Catal. Today. 175 (2011) 293–298.
[12] M.R. Rakshit, K. Mandal, ACS Appl. Mater. Interfaces 6 (2014) 4903–4910.
[13] N. Zhang, Y.J. Xu, CrystEngComm 18 (2016) 24–37.
[14] N. Zhang, M.Q. Yang, S.Q. Liu, Y.G. Sun, Y.J. Xu, Chem. Rev. 115 (2015) 10307–10377.
[15] M.Q. Yang, Y.J. Xu, Chem. Soc. Rev. 43 (2014) 8240–8254.
[16] Q.J. Xiang, J.G. Yu, M. Jaroniec, Chem. Soc. Rev. 41 (2012) 782–796.
[17] N. Zhang, Y.H. Zhang, Y.J. Xu, Nanoscale 4 (2012) 5792–5813.
[18] M.Q. Yang, Y.J. Xu, Phys. Chem. Chem. Phys. 15 (2013) 19102–19118.
[19] S.Q. Liu, B. Xiao, L.R. Feng, S.S. Zhou, Z.G. Chen, C.B. Liu, F. Chen, Z.Y. Wu, N. Xu, W.C. Oh, Z.D. Meng, Carbon 64 (2013) 197–206.
[20] Y. Hou, X.Y. Lia, Q.D. Zhao, G.H. Chen, Appl. Catal. B. 142–143 (2013) 80–88.
[21] Y.J. Yao, Y.M. Cai, F. Lu, F.Y. Wei, X.Y. Wang, S.B. Wang, J. Hazard. Mater. 270 (2014) 61–70.
[22] Y.S. Fu, Q. Chen, M.Y. He, Y.H. Wan, X.Q. Sun, H. Xia, X. Wang, Ind. Eng. Chem. Res. 51 (2012) 11700–11709.
[23] L. Gan, S.M. Shang, C.W.M. Yuen, S.X. Jiang, E.L. Hu, Appl. Surf. Sci. 351 (2015) 140–147.
[24] J.F. Shen, X.F. Li, W.S. Huang, N. Li, M.X. Ye, J. Mater. Res. 29 (2014) 2211–2219.
[25] N. Zhang, M.Q. Yang, Z.R. Tang, Y.J. Xu, ACS Nano 8 (2014) 623–633.
[26] X.Z. Li, N. Zhang, Y.J. Xu, ChemCatChem 7 (2015) 2047–2054.
[27] Y. Wang, J.G. Yu, W. Xiao, Q. Li, J. Mater. Chem. A. 2 (2014) 3847–3855.
[28] L. Xu, F.Y. Zhang, X.Y. Song, Z.L. Yin, Y.X. Bu, J. Mater. Chem. A. 3 (2015) 5923–5933.
[29] L. Zhang, L.H. Du, X. Yu, S.Z. Tan, X. Cai, P.H. Yang, Y. Gu, W.J. Mai, ACS Appl. Mater. Interfaces 6 (2014) 3623–3629.
[30] C. Han, M.Q. Yang, N. Zhang, Y.J. Xu, J. Mater. Chem. A. 2 (2014) 19156–19166.
[31] X. Pan, Y.J. Xu, ACS Appl. Mater. Interfaces 6 (2014) 1879–1886.
[32] X.H. Zhao, X. Liu, RSC Adv. 5 (2015) 79548–79555.
[33] Q. Xiao, Z. Liu, A. Bo, S. Zavahir, S. Sarina, S. Bottle, J.D. Riches, H.Y. Zhu, J. Am. Chem. Soc. 137 (2015) 1956–1966.
[34] X.J. Lang, X.D. Chen, J.C. Zhao, Chem. Soc. Rev. 43 (2014) 473–486.
[35] Z. Wang, X. Zhang, Y. Li, Z.T. Liu, Z.P. Hao, J. Mater. Chem. A. 1 (2013) 6393–6399.
[36] S.F. Chen, H.Q. Wang, L.J. Zhu, J.F. Li, J.F. Sun, Appl. Surf. Sci. 321 (2014) 86–93.
[37] A. Sadezky, H. Muckenhuber, H. Grothe, R. Niessner, U. Poschl, Carbon 43 (2005) 1731–1742.
[38] S. Stankovich, D.A. Dikin, R.D. Piner, K.A. Kohlhaas, A. Kleinhammes, Y.Y. Jia, Y. Wu, S.T. Nguyen, R.S. Ruoff, Carbon 45 (2007) 1558–1565.
[39] H.C. Schniepp, J.L. Li, M.J. McAllister, H. Sai, M. Herrera-Alonso, D.H. Adamson, R.K. Prudhomme, R. Car, D.A. Saville, I.A. Aksay, J. Phys. Chem. B 110 (2006) 8535–8539.
[40] J.W. Xiao, G.L. Xu, S.G. Sun, S.H. Yang, Part. Part. Syst. Charact. 30 (2013) 893–904.
[41] N. Ballarini, F. Cavani, S. Passeri, L. Pesaresi, A.F. Lee, K. Wilson, Appl. Catal. A: Gen. 366 (2009) 184–192.
[42] P.B. Liu, Y. Huang, X. Sun, Mater. Lett. 112 (2013) 117–120.
[43] P.Y. Dong, Y.H. Wang, B.C. Cao, S.Y. Xin, L.N. Guo, J. Zhang, F.H. Li, Appl. Catal. B 132 (2013) 45–53.
[44] T.G. Xu, L.W. Zhang, H.Y. Cheng, Y.F. Zhu, Appl. Catal. B 101 (2011) 382–387.
[45] X.F. Yang, J.L. Qin, Y. Jiang, R. Li, H. Tang, Appl. Catal. B 166 (2015) 231–240.
[46] A.R. Park, K. Zhang, J.H. Park, P.J. Yoo, ACS Appl. Mater. Interfaces 4 (2012) 3893–3901.
[47] L. Zhang, L.H. Du, X. Yu, S.Z. Tan, X. Cai, W.J. Mai, ACS Appl. Mater. Interfaces 6 (2014) 3623–3629.
[48] F. Wang, C.H. Li, H.J. Chen, R.B. Jiang, L.D. Sun, J.C. Yu, C.H. Yan, J. Am. Chem. Soc. 135 (2013) 5588–5601.
[49] Z.F. Jiao, Z.Y. Zhai, X.N. Guo, X.Y. Guo, J. Phys. Chem. C 119 (2015) 3238–3243.
[50] S.S. Soni, D.A. Kotadia, Catal. Sci. Technol. 4 (2014) 510–515.
[51] K. Sharma, M. Kumar, V. Bhalla, Chem. Commun. 51 (2015) 12529–12532.
[52] G.M. Scheuermann, L. Rumi, P. Steurer, W. Bannwarth, R. Mülhaupt, Green Chem. 16 (2014) 331–341.
[53] H. Zhang, L.H. Guo, D.B. Wang, L.X. Zhao, B. Wan, ACS Appl. Mater. Interfaces 7 (2015) 1816–1823.
[54] G.M. Scheuermann, L. Rumi, P. Steurer, W. Bannwarth, R. Mülhaupt, J. Am. Chem. Soc. 131 (2009) 8262–8270.
[55] Y.Q. Luo, S.S. Fan, N.Y. Hao, S.L. Zhong, W.C. Liu, CrystEngComm 17 (2015) 503–506.
[56] L. Yin, J. Liebscher, Chem. Rev. 107 (2007) 133–173.
[57] Á. Molnár, Chem. Rev. 111 (2011) 2251–2320.
[58] L.Y. Ding, R.J. Wei, H. Chen, J.C. Hu, J.L. Li, Appl. Catal. B 172–173 (2015) 91–99.
[59] H.Y. Zhua, R. Jiang, S.H. Huang, J. Yao, F.Q. Fu, J.B. Li, Ceram. Int. 41 (2015) 11625–11631.
[60] W.G. Wang, J.G. Yu, Q.J. Xiang, B. Cheng, Appl. Catal. B 119 (2012) 109–116.
[61] H.T. Li, Z.H. Kang, Y. Liu, S.T. Lee, J. Mater. Chem. 22 (2012) 24230–24253.
[62] D.F. Zhang, X.P. Pu, K.P. Du, Y.M. Yu, Sep. Purif. Technol. 137 (2014) 82–85.
[63] L.L. Tan, W.J. Ong, S.P. Chai, A.R. Mohamed, Appl. Catal. B. 166 (2015) 251–259.
[64] T. Tachikawa, M. Fujitsuka, T. Majima, J. Phys. Chem. C 111 (2007) 5259–5275.
[65] C. Deraedt, A.D. Didier, Acc. Chem. Res. 47 (2014) 494–503.
[66] S. Sarina, H. Zhu, E. Jaatinen, Q. Xiao, H. Liu, J.F. Jia, C. Chen, J. Zhao, J. Am. Chem. Soc. 135 (2013) 5793–5801.
[67] S.T. Gao, N.Z. Shang, C. Feng, C. Wang, Z. Wang, RSC Adv. 4 (2014) 39242–39247.
[68] Q. Xiao, S. Sarina, A. Bo, J.F. Jia, H.W. Liu, D.P. Arnold, Y.M. Huang, H.S. Wu, H.Y. Zhu, ACS Catal. 4 (2014) 1725–1734.
[69] Q. Xiao, S. Sarina, E. Jaatinen, J.F. Jia, D.P. Arnold, H.W. Liu, H.Y. Zhu, Green Chem. 16 (2014) 4272–4285.